Materials Advances

ROYAL SOCIETY OF CHEMISTRY

PAPER

View Article Online
View Journal

Cite this: DOI: 10.1039/d6ma00290k

Evaluation of pressure induced physical and magnetic properties of A_3CrO_4 (A = Mg, Ca, Sr) alkali–metal oxides for spintronics applications *via* DFT

Md. Rony Hossain, *[ab] Mst. Shamima Khanom,[b] Prianka Mondal,[c] Akash Kumer Paul[b] and Farid Ahmed[b]

The present study employs density functional theory (DFT) within the CASTEP framework to systematically investigate the pressure-tunable structural, electronic and magnetic properties of A_3CrO_4 (A = Mg, Ca, Sr) alkali–metal oxides using GGA-PBE, GGA+U and GGA-PBEsol functionals. Structural optimization confirms that all A_3CrO_4 (A = Mg, Ca, Sr) compounds crystallize in the cubic $Pm\bar{3}m$ space group, with ferromagnetic (FM) ordering consistently more stable than non-magnetic (NM) states across the entire pressure range of 0–30 GPa. Mg_3CrO_4 and Ca_3CrO_4 exhibit robust FM ground states with total magnetic moments of +4.0 to −4.1μ_B maintaining half-metallicity under hydrostatic pressures up to 30 GPa. In contrast, Sr_3CrO_4 undergoes a pressure-induced magnetic phase transition, with its magnetic moment reversing sign at 20–30 GPa, indicating a shift toward antiferromagnetic (AFM) or ferrimagnetic ordering. Elastic constant analysis confirms dynamic stability across the entire pressure range (0–30 GPa). While Mg_3CrO_4 remains brittle under compression, Ca_3CrO_4 and Sr_3CrO_4 exhibit pressure-induced ductility transitions, transforming from brittle to ductile behavior at higher pressures. Electronic structure calculations reveal persistent half-metallicity, with spin-down channels retaining wide band gaps and spin-up channels displaying metallic behavior. The application of Hubbard corrections (GGA+U) further validates the robustness of the electronic properties. The average sound velocity, Debye temperature, Debye frequency, melting temperature and Gruneisen parameter were analyzed under pressures of up to 30 GPa. Mg_3CrO_4 and Ca_3CrO_4 show a steady increase in sound velocity, Debye temperature, and frequency, indicating lattice stiffening, stronger bonding and enhanced thermal stability. In contrast, Sr_3CrO_4 exhibits anomalous behavior, with values rising up to 20 GPa but slightly decreasing at 30 GPa, consistent with its pressure-induced magnetic reversal. Melting temperatures increase significantly for all compounds, confirming their suitability for high-temperature and high-pressure applications. The interplay between pressure and functional analysis in these Cr-based compounds provides valuable insights for advancing spintronics and functional materials design.

Received 3rd March 2026,
Accepted 27th April 2026

DOI: 10.1039/d6ma00290k

rsc.li/materials-advances

1. Introduction

Spintronics, an emerging field, utilizes an electron's intrinsic spin in addition to its charge to store, process, and transmit information, offering the potential for faster, smaller, and more energy-efficient devices compared to conventional electronics.[1–3] This discipline is fundamentally driven by materials exhibiting high spin polarization, prolonged spin coherence times, and robust half-metallicity, particularly at room temperature.[2,4] Half-metallic ferromagnets (HMFs) are particularly attractive due to their unique electronic structure, where one spin channel is metallic while the other is semiconducting, leading to 100% spin polarization at the Fermi level.[5] This property makes half-metals ideal candidates for generating fully spin-polarized currents, which are essential for high-efficiency spintronic devices such as magnetic tunnel junctions (MTJs), spin valves, and spin-based transistors. A recent study proposed single-molecule optoelectronic devices using half-metallic FeN_4-doped armchair graphene nanoribbons as electrodes coupled with metalloporphyrin molecules, achieving excellent spin-filtering effects through photo galvanic mechanisms.[6] The surface stability of half-metallicity is critical for device performance, as demonstrated in CrYCoAl, where

[a] Department of Software Engineering, Daffodil International University, DSC, Birulia, Savar, Dhaka, 1216, Bangladesh. E-mail: rony.hossainb@gmail.com
[b] Department of Physics, Jahangirnagar University, Savar, Dhaka, 1342, Bangladesh
[c] Dhaka University of Engineering & Technology, Gazipur, 1707, Bangladesh

surface effects were analyzed to ensure high spin polarization in thin-film configurations essential for MTJs.[7] Furthermore, 2D half-metallic systems such as $MnAsS_4$ and $MnXSe_4$ (X = As, Sb) exhibit intrinsic ferromagnetism with large spin gaps (up to 1.46 eV) and high Curie temperatures, addressing the long-standing challenge of thermal stability in nanoscale spintronic devices.[8] This characteristic makes half-metallic compounds highly promising for advanced spintronic and quantum information technologies such as spintronic applications,[9] including magnetic tunnel junctions,[10] spin injection systems,[11] magnetic data storage devices[12] and nonvolatile magnetic random-access memory technologies.[13]

Since the advent of spintronics in the early 1980s,[14] half-metallic ferromagnetic (HMF) materials have garnered significant attention in both theoretical and experimental domains of materials science. The half-metallic nature was initially identified by de Groot and collaborators in semi-Heusler alloys such as NiMnSb and PtMnSb, marking a foundational advancement in spin-dependent electronic materials.[14] Subsequent computational and experimental investigations have identified half-metallic behavior in a wide range of compounds beyond the initial semi-Heusler systems. Notable examples include rutile-type TiO_2,[15] spinel $FeCr_2O_4$,[16] full Heusler Ti_2CoSi,[17] quadruple oxide perovskite $CaCu_3Fe_2Re_2O_{12}$,[18] double perovskites La_2CrNiO_6,[19] Sr_2MnTaO_6,[20] Ba_2YbTaO_6,[21] multiferroics RuC_{l2}/Al_2S_3,[22] $RuBrF/Sc_2CO_2$[23] zintl compounds $EuMg_2X_2$ (X = Sb and Bi)[24] and XCr_2Bi_2 (X = Ca, Sr).[25] Benjamin Balke *et al.*[26] conducted a comprehensive study on the C 1b compound $CoTi_{1-x}M_xSb$ (M = Fe, Mn, Cr, V) combining experimental techniques with first-principles calculations to demonstrate that selective substitution with 3d transition metals induces tunable half-metallic ferromagnetism, maintains crystalline stability, and achieves high Curie temperatures (>700 K) thereby highlighting the material's potential for spintronic applications. Seungho Seong *et al.* employed XMCD and XAS to investigate temperature-dependent mixed-valent states of Cr ions in CrO_2 nanorods, providing direct experimental evidence of its half-metallic ferromagnetism.[27] Recently, Samira Barouni *et al.* synthesized a nanoscale semiconductive perovskite, $La_{0.25}Sr_{0.75}Sn_{0.4}In_{0.25}Ru_{0.35}O_3$ (LSSIRuO), *via* co-doping of $SrSnO_3$, demonstrating a narrowed band gap of 1.3 eV, robust conductivity, and low-temperature ferromagnetic ordering-highlighting its potential for optoelectronic, memory, and spintronic applications.[28] Rasik Ahmad Parray *et al.* investigated a nanocrystalline Cr_2NiAl inverse Heusler alloy synthesized *via* mechanical alloying, revealing a face-centered cubic X_A/X_α structure, aggregated morphology, tunable electronic behavior, room-temperature soft ferromagnetism, and improved magnetic properties with higher annealing temperatures.[29]

Transition metal oxides, especially those with perovskite or related structures, have garnered significant attention due to their tunable electronic and magnetic properties.[30–32] Chromium dioxide (CrO_2), a well-known half-metallic ferromagnet, is a promising candidate for such applications due to its high Curie temperature and full spin polarization, though surface degradation remains a challenge.[33] Similarly, other chromium-based compounds such as $ZnCrO_4$ perovskites and Cr_2O_3 have been studied for their half-metallic ferromagnetism and spintronic applications.[31,34] The precise engineering of these properties is crucial for advancing spintronic devices.[35] Mohammed El Amine Monir *et al.*[36] investigated X_3FeO_4 (X = Mg, Ca, Sr) using DFT, revealing ferromagnetic stability, semi-metallic behavior, and half-metallicity supported by elastic, electronic, and magnetic analyses. Their study also reported thermal parameters such as expansion coefficient, heat capacity, and Debye temperature, confirming the compounds' potential for advanced applications.

The objective of this study is to demonstrate the half-metallic nature of alkaline-earth chromates X_3CrO_4 (X = Mg, Ca, Sr) by analyzing their structural, electronic, and magnetic properties using DFT within the CASTEP framework under hydrostatic pressures ranging from 0 to 30 GPa. A central motivation is to investigate how the half-metallic gap evolves with applied pressure in Mg_3CrO_4, Ca_3CrO_4, and Sr_3CrO_4 employing GGA-PBE, GGA-PBEsol and GGA+U functionals. Understanding how variations in the alkaline-earth cation at the A-site influence these properties under pressure is key to designing new materials with enhanced performance for opto-spintronic applications. The paper is organized into the following sections: Computational details: outlines the methodology, Results and discussion: presents and interprets the structural, elastic, electronic, and magnetic findings, and Conclusions: summarizes the main outcomes.

2. Computational details

DFT-based CASTEP computer software with the generalized gradient approximation (GGA) was used for first-principles calculations. The Perdew–Burke–Ernzerhof (PBE) exchange–correlation functional with projected augmented-wave (PAW) pseudopotentials was selected for this calculation.[37–39] In the calculation of lattice optimization, the convergence parameters were set as follows: (i) the maximum ionic displacement was 0.002 Å, (ii) the maximum stress component was 0.10 GPa, and (iii) 0.05 eV $Å^{-1}$ was set as the maximum ionic force. The electromagnetic wave function extension in a plane-wave basis set uses an energy cut-off of 500 eV, and the Brillouin zone is sampled using $8 \times 8 \times 8$ *k*-points for all calculations. The application of the Broyden has optimized the geometric structure using the Fletcher–Goldfarb–Shanno (BFGS) minimization technique.[40] The adopted Hubbard parameter $U = 2.5$ eV for the Cr 3d orbitals is consistent with previously reported DFT+*U* studies on chromium-based compounds, where comparable values $U = 2.5$ eV for Cr in chromium carbides have been successfully employed to describe the localized 3d electrons of Cr.[41] The Vanderbilt-type ultrasoft pseudopotential (UPP) formalism was used to analyze the interactions between valence electrons and ions. UPPs achieve a substantially softer pseudo-wave function, requiring a significant reduction in plane waves for calculations with the same level of precision.[42] Additionally, spin polarization was only applied to the magnetic state material in the comparison material used in the lowest energy

computation, and spin polarization was not applied to the non-magnetic state material in all other computations. The elastic constants were determined using first-principles computations by carrying out a sequence of specified homogeneous distortions with finite parameters and calculating the resulting stress concerning optimizing the interior atomic freedom. With an upper limit of 0.5%, each strain element had three positive and three negative amplitudes. After that, the calculated stress as a function of strain was fitted linearly to obtain the parameters of the elastic modulus. To facilitate the calculation of the optical properties for a dense mesh of evenly distributed *k*-points, the BZ integration was performed using a 12 × 12 × 12 MP *k*-mesh.

2.1 Structural properties and structural stability

A_3CrO_4 (A = Mg, Ca, Sr) is structured in the cubic $Pm\bar{3}m$ space group shown in Fig. 1. The Wyckoff positions 3c $(0, \frac{1}{2}, \frac{1}{2})$, 1a (0, 0, 0), 3d $(0, 0, \frac{1}{2})$ and 1b $(\frac{1}{2}, \frac{1}{2}, \frac{1}{2})$ in this crystal structure are occupied by A, B, O1 and O2 atoms, respectively.[43] These structures are optimized in ferromagnetic (FM) and non-magnetic (NM) states to verify the most stable state. The Birch–Murnaghan equation of state (EOS) is a fundamental model used to describe the pressure–volume relationship of materials, particularly under high-pressure conditions, by expanding the solid's free energy as a polynomial in the Eulerian finite strain. The standard third-order Birch–Murnaghan EOS is well-defined for cubic materials.[44] The present materials were simulated in FM and NM magnetic configurations in various exchange functionals to extract the ground state structural parameters by performing a least-squares fit of the crystal energy against the unit cell volume through the Birch–Murnaghan equation of state,[45]

$$E(V) = E_0 + \left(\frac{9B_0V_0}{16}\right) \times \left\{\left[\left(\frac{V_0}{V}\right)^{\frac{2}{3}} - 1\right]B_0' + \left[\left(\frac{V_0}{V}\right)^{\frac{2}{3}} - 1\right]^2\left[6 - 4\left(\frac{V_0}{V}\right)^{\frac{2}{3}}\right]\right\} \quad (1)$$

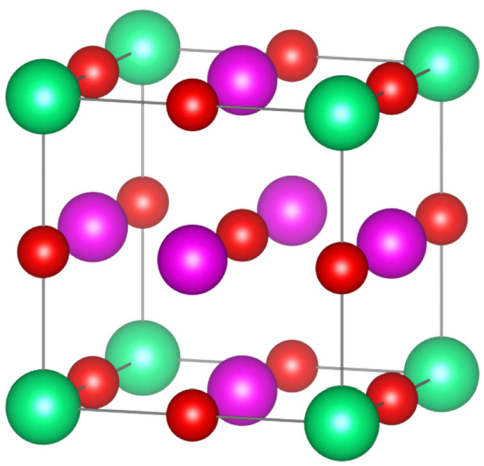

Fig. 1 Crystal structure of cubic A_3CrO_4 compounds (A = Mg, Ca, Sr).

The terms $E(V)$, V and B_0 (B_0') in this equation represent the ground state energy, unit cell volume, and the bulk modulus (pressure derivate of the bulk modulus), respectively. For all the compounds the optimized energy-volume curve in these different phases clearly indicates that the FM phase is significantly most stable as it holds the lowest energy in all approximations rather than the NM phase, as depicted in Fig. 3(a–i).

Variations in lattice parameters arise from the distinct treatment of the exchange–correlation term by different functionals. Hence, A_3CrO_4 (A = Mg, Ca, Sr) was geometrically optimized with GGA-PBE, GGA+U and GGA-PBEsol functionals and the values are reported in Table 3. As shown in Fig. 2(a and b), hydrostatic pressure strongly influences the lattice parameters and unit cell volumes across PBE, PBEsol and GGA+U calculations. Increasing pressure gradually reduces the lattice parameters by shortening interatomic distances. From Fig. 2(c), the lattice constant reductions are modest with GGA-PBEsol consistently predicting slightly lower compressibility relative to GGA-PBE and GGA+U. In Fig. 2(d) the volume reduction is significantly higher across all functionals. This comparative analysis highlights that while lattice constants provide a direct measure of contraction, volume reductions offer a more sensitive indicator of bulk compressibility, and functional choice introduces systematic variations that must be considered in high-pressure predictions.

Any deviance from the optimal cubic structure can be assessed by the tolerance factor (t) that typically ranges from 0.81 to 1.11 for cubic perovskites.[47] The Goldschmidt tolerance factor, t, is given as,

$$t = 0.707\frac{r_A + r_O}{\{r_{Cr} + r_O\}} \quad (2)$$

where r_A, r_O, and r_{Cr} represent the atomic radius of the A-site atom (A = Mg, Ca, Sr), O atom, and Cr atom, respectively, which are calculated by using Shannon's effective ionic radii and the values t of these are depicted in Table 2. Deviation of the tolerance factor from unity reduces the likelihood of stabilizing a cubic phase and instead favors the formation of less symmetric structures. The calculated t-values for A_3CrO_4 (A = Mg, Ca, Sr) perovskites (Table 1) confirm the stability of the cubic structure.

2.2 Electronic properties

After completing the geometric optimization of A_3CrO_4 compounds (A = Mg, Ca, Sr) under hydrostatic pressures (0–30 GPa), it is crucial to analyze their electronic structures to determine whether they exhibit half-metallic characteristics and to assess their suitability for photoelectric and optoelectronics applications.[48] Band structure and density of states (DOS) calculations provide essential insights into electron dispersion, band gap properties and orbital contributions that influence optical absorption, carrier transport and radiative efficiency.[49]

Fig. 4 illustrates the band structures of A_3CrO_4 compounds (A = Mg, Ca, Sr) obtained using two different exchange–correlation functionals along high-symmetry paths. Across the entire pressure range (0–30 GPa), the spin down channel shows a wide

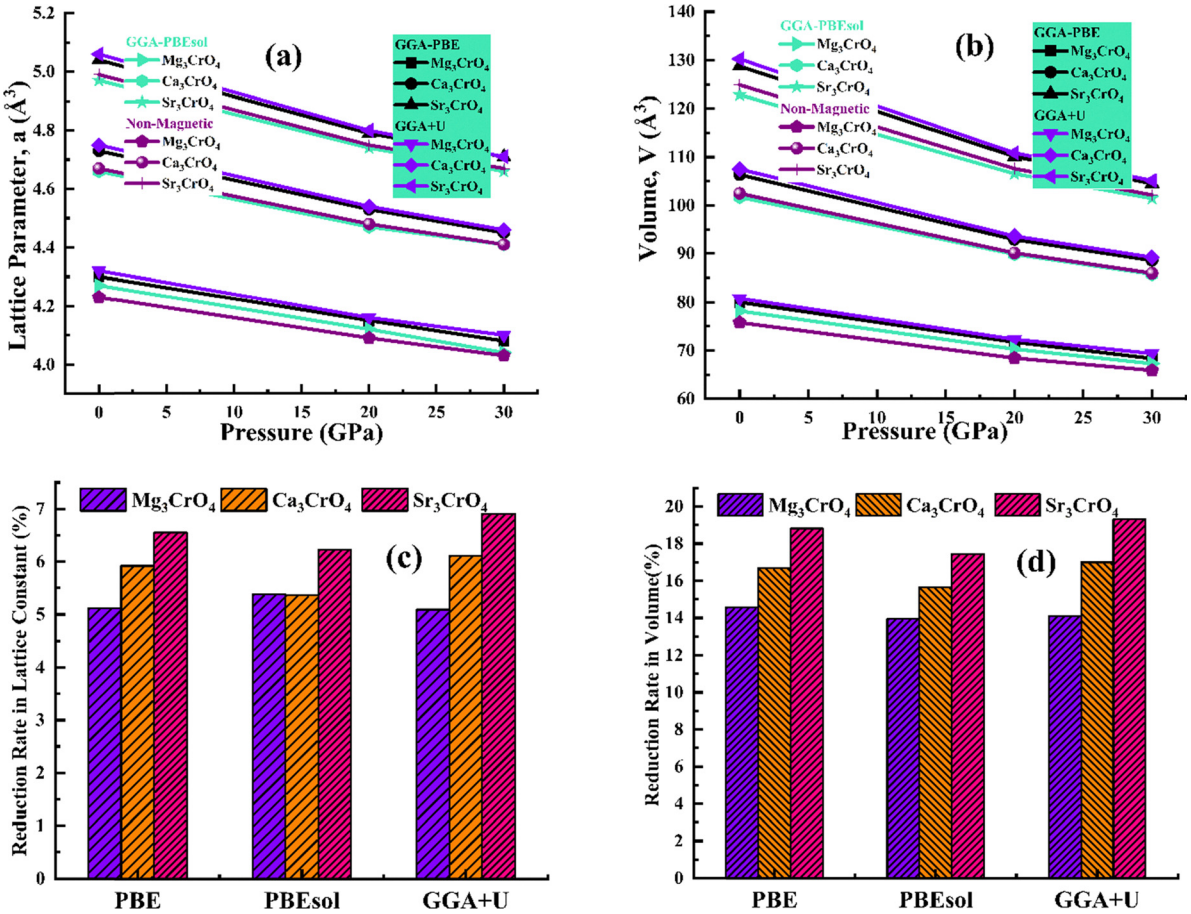

Fig. 2 (a–d) Change in the lattice parameters and volume of cubic A_3CrO_4 compounds (A = Mg, Ca, Sr) under pressure (0–30 GPa) with different functionals.

semiconducting band gap. In contrast, in the spin up channel the valence conduction bands merge in the Fermi level confirming the metallic nature. Both show the half metallic nature of our investigated compounds.

When the Hubbard correction GGA+U is applied, the band gap increases reflecting the tendency of semi-local GGA to underestimate band gaps and the improved accuracy of GGA+U. The systematic increase in band-gap values from GGA-PBE to GGA+U highlights the intrinsic limitation of semi-local functionals in underestimating band gaps because of the absence of derivative discontinuity in the exchange potential.[50] The consistent GGA/GGA+U trend observed here confirms the robustness of the electronic structure calculations and supports the reliability of the predicted half metallic behavior of the A_3CrO_4 compounds (A = Mg, Ca, Sr) and hybrid functionals provide more accurate band-gap estimations, which are computationally demanding, making them less practical for large-scale property calculations on standard computing platforms. In contrast, GGA-PBE offers a good balance between efficiency and accuracy, and thus was used for all subsequent calculations, while GGA+U was employed primarily for band-gap correction and validation.

The total density of states (TDOS) describes the distribution of electronic energy levels per unit interval and serves as a key indicator of the overall electronic structure of a material.[51] Fig. 5 shows the TDOS of the A_3CrO_4 compounds calculated using the GGA functional. All the investigated systems exhibit ferromagnetic ground states across the studied pressure range, where the spin-up channel exhibits metallic behavior and the spin-down channel is semiconducting, except for Sr_3CrO_4 at 30 GPa, where the characteristics are reversed, confirming its antiferromagnetic nature as evidenced by the Fermi level position. The unequal contributions from the two spin channels further validate their magnetic behavior. In addition, the TDOS reveals the band gaps of these compounds, which are consistent with the corresponding band structure results.

2.3 Spin magnetic moments

At $T = 0$ K, the spin-polarized computation directly obtains the magnetic moment. Utilizing the actual magnetic moments per formula unit, the magnetic moment is calculated as follows,

$$\mu = 4O_{oxygen} + Cr + 3A\ (Mg, Ca, Sr) \quad (3)$$

Table 4 provides the spin magnetic moments μ_B for A-site cations (A = Mg, Ca, Sr), chromium (Cr) and oxygen (O) anions in the A_3CrO_4 family under varying hydrostatic pressures (0, 20, 30 GPa) and using three distinct functionals GGA-PBE, GGA-

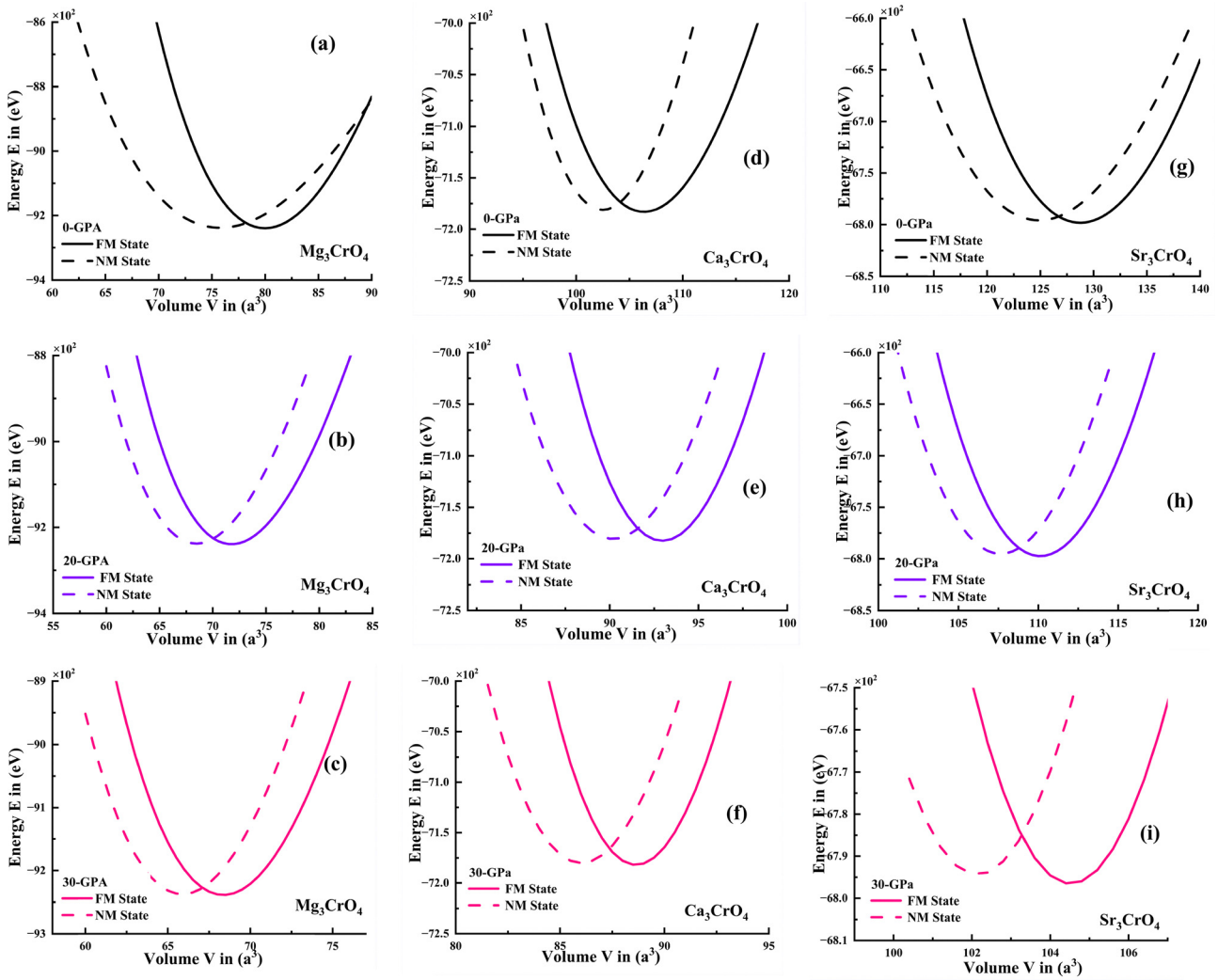

Fig. 3 Energy *versus* volume curve (a)–(i) for A_3CrO_4 compounds (A = Mg, Ca, Sr) under hydrostatic pressures (0–30 GPa) for FM (ferromagnetic) and NM (non-magnetic state).

Table 1 A summary of the chosen parameters for the DFT-calculations performed in the present work

Category	Cubic Values of descriptions
Convergence	Energy tolerance: 1.0×10^{-6} a.u.; force tolerance: 1.0×10^{-4} a.u.
Exchange-correction functionals	PBE-GGA (Perdew–Burke–Ernzerhof), GGA-PBEsol and GGA+U
Plane-wave cutoffs	500 eV
Smearing section	Occupations = smearing; method = Gaussian; width = 0.10 eV
K-points grid	$8 \times 8 \times 8$
Pseudopotentials	OTFG ultrasoft
Relativistic treatment	Koelling–Harmon
Spin treatment	Spin polarized (FM calculations)
Electronic minimization	Metallic treatment with density mixing; Pulay mixing scheme
Geometry optimization	Method = BFGS; max steps = 1000; force tolerance = 0.05 eV $Å^{-1}$; stress tolerance = 0.1 GPa

PBEsol and GGA+U. These calculations provide critical insights into the magnetic behavior of these chromate perovskite-related materials and their potential for spintronic applications, especially under pressure-induced modifications. Understanding these properties is vital for the design of materials with tunable magnetic responses.[52,53] For Mg- and Ca-based compounds the data consistently indicate a ferromagnetic (FM) alignment with positive total magnetic moments

Table 2 Ground-state structural parameters of A_3CrO_4 (A = Mg, Ca, Sr): lattice constant (a, Å), volume (V, Å^3), crystal energy (E_0, eV), bulk modulus (B, GPa) and tolerance factor (t) under pressure (0–30 GPa)

		Mg_3CrO_4			Ca_3CrO_4			Sr_3CrO_4		
		0 GPa	20 GPa	30 GPa	0 GPa	20 GPa	30 GPa	0 GPa	20 GPa	30 GPa
GGA-PBE (FM-state)	Lattice constant a (Å)	4.30	4.15	4.08	4.73	4.53	4.45	5.04	4.79	4.71
	Volume V (Å^3)	79.98	71.76	68.36	106.36	92.96	88.64	128.75	110.12	104.52
	Energy E (eV)	−9239.78	−9239.36	−9238.86	−7183.08	−7182.47	−7181.82	−6798.26	−6797.44	−6796.60
	Bulk modulus B (GPa)	124.14	156.87	228.97	97.95	278.87	418.62	90.50	232.08	371.48
GGA-PBE (NM-state)	Lattice constant a (Å)	−9238.4	−9238.03	−9237.64	−7181.15	−7180.59	−7179.97	−6795.90	−6795.21	−6794.39
	Volume V (Å^3)	4.23	4.09	4.03	4.67	4.48	4.41	4.99	4.75	4.67
	Energy E (eV)	75.77	68.45	65.89	102.48	90.18	86.02	124.88	107.64	102.15
	Bulk modulus B (GPa)	96.82	536.12	815.04	140.92	232.05	338.43	68.32	227.22	368.05
	Tolerance factor	0.82			0.92			0.99		
		Mg_3FeO_4			Ca_3FeO_4			Sr_3FeO_4		
Other calculation	Lattice constant a (Å)	4.28[46]			4.74[46]			5.03[46]		
	Energy E (Ry)	−4350.39[46]			−7230.82[46]			−22 227.41[46]		
	Bulk modulus B (GPa)	152.003[46]			108.95[46]			94.36[46]		

Table 3 Percentage reduction in lattice constant (a, Å) and unit cell volume (V, Å^3) for Mg_3CrO_4, Ca_3CrO_4 and Sr_3CrO_4 from 0 to 30 GPa calculated using different functionals

		Mg_3CrO_4			Ca_3CrO_4			Sr_3CrO_4		
Functional dependence	Lattice constant reduction in %	GGA-PBE 5.12	GGA-PBEsol 5.38	GGA+U 5.09	GGA-PBE 5.92	GGA-PBEsol 5.36	GGA+U 6.11	GGA-PBE 6.55	GGA-PBEsol 6.23	GGA+U 6.91
	Volume reduction in %	GGA-PBE 14.56	GGA-PBEsol 13.94	GGA+U 14.11	GGA-PBE 16.67	GGA-PBEsol 15.65	GGA+U 16.99	GGA-PBE 18.82	GGA-PBEsol 17.44	GGA+U 19.31

approximately +4μ_B to +4.1μ_B observed across all pressures and DFT functionals. This behavior is consistent with Cr^{3+} (d^3, high-spin, S = 3/2) ions, where the magnetic moments of the Cr and O atoms align to produce a net ferromagnetic state. Such ferromagnetic coupling in chromite is often mediated by super-exchange interactions and hybridization effects.[54–56] The A-site cations (Mg and Ca) exhibit small positive magnetic moments, while the Cr ions contribute the dominant positive moment, generally ranging from 3.18μ_B to 3.78μ_B, depending on the specific compound, pressure and functional. The oxygen anions also contribute positive moments, suggesting a degree of spin polarization induced by their interaction with the Cr ions.

In contrast, Sr_3CrO_4 exhibits a notable and intriguing pressure-induced magnetic transition. At 0 GPa, under the GGA-PBE functional Sr_3CrO_4 shows a positive total magnetic moment of approximately +4μ_B. However, as pressure increases to 20 GPa and further to 30 GPa, the total magnetic moments reverse sign, becoming approximately −4μ_B and −4.01μ_B respectively under the GGA-PBE and GGA-PBEsol functionals, as demonstrated in Fig. 6. This sign reversal suggests a shift from an initial ferromagnetic ordering to an antiferromagnetic (AFM) or ferrimagnetic ordering where the dominate magnetic moments align antiparallel to their initial orientation.[57] This transition is particularly significant as it implies that the magnetic properties of Sr_3CrO_4 can be manipulated by external pressure, offering potential avenues for mechanically controlled spin or switchable spintronics materials.[58] Such pressure-driven transitions have been observed in other transition metal oxides, impacting their electronic and magnetic structures.[54,59] The phenomenon in Sr_3CrO_4 is similar to pressure-induced spin-state transitions in iron-based oxides, which can lead to novel functionalities.[60]

In Table 4, GGA+U generally yields more stable positive magnetic moments for all compounds with the total magnetic moments consistently around +4μ_B to +4.1μ_B. This suggests that the on-site Coulomb correction stabilizes the high spin d^3 state of Cr^{3+} making it less susceptible to charge transfer effects or spin collapse under pressure.[61,62] For Sr_3CrO_4, while PBE and PBEsol show a moment reversal, GGA+U consistently maintains a positive magnetic moment across all pressures indicating a more robust ferromagnetic state predicted by this functional. This highlights the importance of accurately treating electron corrections in such systems, as the magnetic ground state can be sensitive to the chosen theoretical framework.

The oxygen anion moments provide further insights into the electron structure and bonding. In Mg_3CrO_4 and Ca_3CrO_4 the positive oxygen moments increase with pressure under GGA-PBE and GGA-PBEsol. This increase reflects enhanced covalency and p–d hybridization between oxygen and chromium under compression. Similar observations have been made in other transition-metal oxides like NiO and CoO, where pressure strengthens the hybridization between oxygen 2p

and transition metal 3d orbitals leading to greater spin polarization of the oxygen sublattice.[63]

In Sr_3CrO_4 however, the oxygen moments also reverse their sign under PBE and PBEsol with increasing pressure,

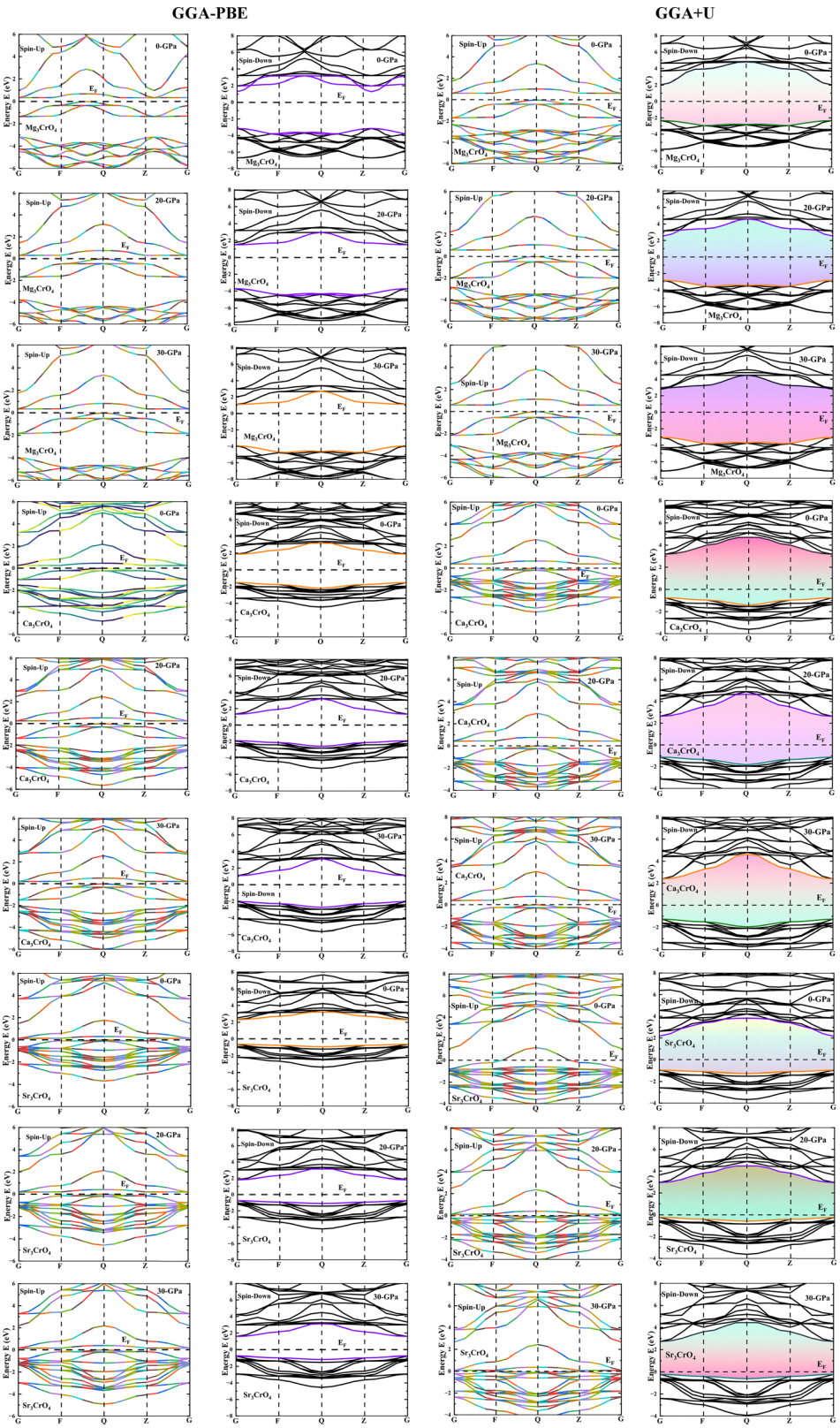

Fig. 4 Band structure of the A_3CrO_4 compounds (A = Mg, Ca, Sr) under hydrostatic pressures (0–30 GPa) for GGA-PBE and GGA+U functionals.

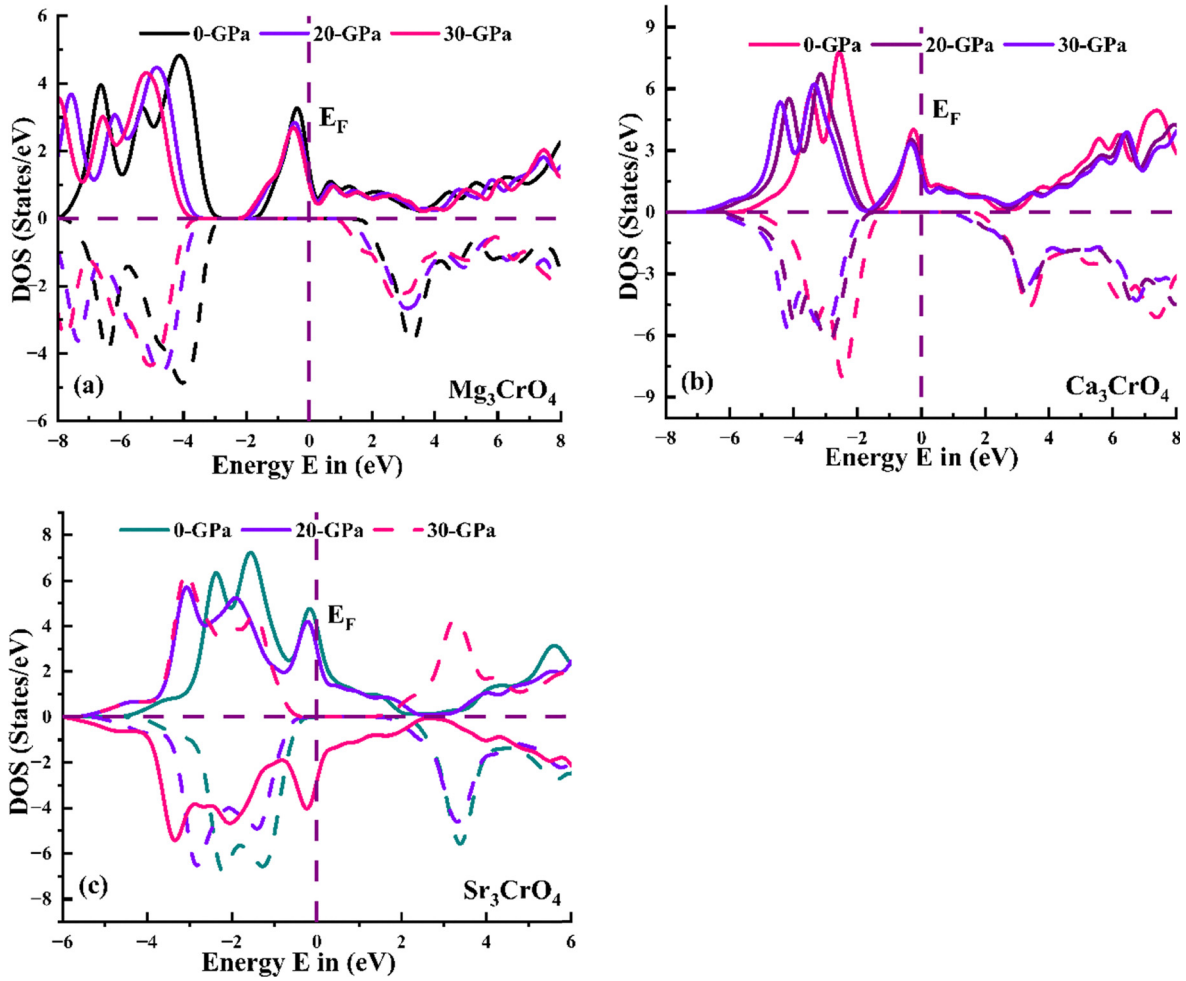

Fig. 5 (a–c) Total density of states (TDOS) of A_3CrO_4 compounds (A = Mg, Ca, Sr) under hydrostatic pressures (0–30 GPa).

Table 4 The calculated magnetic moments μ_B for cubic A_3CrO_4 compounds (A = Mg, Ca, Sr) under hydrostatic pressures (0–30 GPa) using different exchange correlation functionals

		Mg_3CrO_4			Ca_3CrO_4			Sr_3CrO_4		
		0 GPa	20 GPa	30 GPa	0 GPa	20 GPa	30 GPa	0 GPa	20 GPa	30 GPa
GGA-PBE	μ_A	0.21	0.21	0.21	0.24	0.30	0.30	0.27	−0.27	−0.30
	μ_{Cr}	3.52	3.45	3.18	3.64	3.53	3.48	3.79	−3.64	−3.59
	μ_O	0.36	0.44	0.44	0.12	0.24	0.28	−0.08	−0.08	−0.12
	μ_{total}	4.09	4.10	3.83	4.00	4.07	4.06	4.00	−3.99	−4.01
GGA-PBEsol	μ_A	0.21	0.21	0.18	0.27	0.30	0.30	−0.27	−0.30	−0.33
	μ_{Cr}	3.50	3.27	3.06	3.60	3.48	3.37	−3.74	−3.60	−3.56
	μ_O	0.36	0.44	0.44	0.16	0.28	0.28	0.04	−0.12	−0.16
	μ_{total}	4.07	3.92	3.68	4.03	4.06	3.95	−3.97	−4.02	−4.05
GGA-GGA+U	μ_A	0.21	0.21	0.24	0.27	0.30	0.30	0.27	0.30	0.30
	μ_{Cr}	3.63	3.54	3.50	3.78	3.65	3.61	3.96	3.78	3.74
	μ_O	0.20	0.32	0.36	0.08	0.04	0.08	−0.32	−0.12	−0.08
	μ_{Total}	4.04	4.07	4.10	4.13	3.99	3.99	3.91	3.96	3.96

aligning with the overall change in the total magnetic moment. This suggests that the oxygen sublattice actively participated in the pressure-induced magnetic transition, rather than merely reflecting the Cr moments. The magnetic properties of Cr-containing perovskites are generally complex due to the competition between direct exchange and super-exchange interactions and the influence of the structural distortions.[64–67]

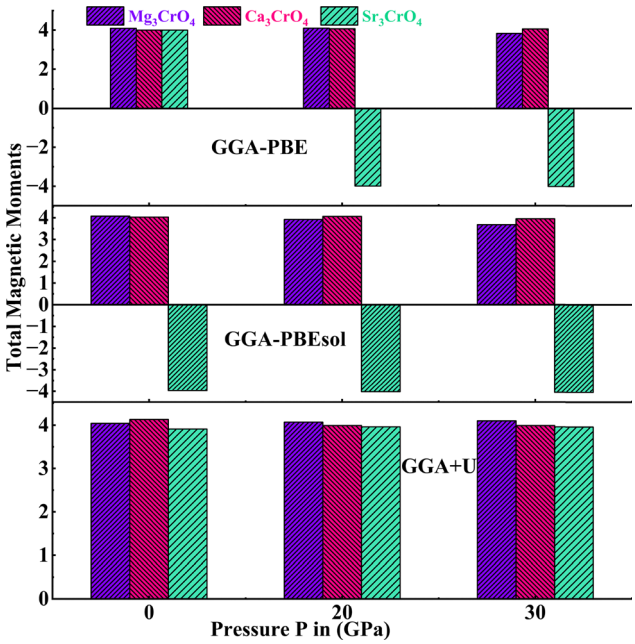

Fig. 6 The magnetic moments μ_B for the cubic A_3CrO_4 compounds (A = Mg, Ca, Sr) under hydrostatic pressures (0–30 GPa) using different exchange correlation functionals.

Overall, materials with tunable spin polarization could be employed in pressure-sensitive magnetic sensors, data storage devices, and spin valves where mechanical strain dictates the magnetic state.[68,69]

2.4 Elastic properties and dynamical stability

Elastic constants are necessary to have a more thorough theoretical comprehension of the characteristics of materials that are determined by the electron–phonon interaction processes and the density of states of phonons. Since the stress–strain curve in many minerals exhibits low nonlinearity, practical applications can assume a linear relationship between stress and strain.[70] Elastic constants can calculate essential physical parameters like melting point, hardness, sound velocities, Debye temperature, and shear modulus. The elastic constants are the total energy second derivative for different lattice deformations. More thorough computations of the total energy are necessary[71] for the elastic constants. The elastic constants can be calculated from the resulting formula,

$$C_{ij} = \frac{1}{V_0}\left(\frac{d^2E}{de_ie_j}\right) \quad (4)$$

where E is the internal energy, V_0 is the equilibrium volume, and e_i and e_j are the stress and strain components.

Since A_3CrO_4 (A = Mg, Ca, Sr) is a cubic structure with a high degree of symmetry, the elastic constant reduces to three independent elastic constants: C_{11}, C_{12}, and C_{44}[72] as reported in Table 5. The following is an expression of the conventional mechanical stability conditions in cubic crystals at equilibrium in terms of elastic constants,[73,74]

$$C_{44} > 0,\ C_{11} > |C_{12}|,\ C_{11} + 2C_{12} > 0 \quad (5)$$

The equations for mechanical stability under pressure are given by,[75]

$$\begin{aligned} &C'_{11} - C'_{12} = (C_{11} - C_{12}) - 2P > 0, \\ &C'_{11} + 2C'_{12} = (C_{11} + 2C_{12}) > 0, \quad C'_{44} = C_{44} - P > 0 \end{aligned} \quad (6)$$

As reported in Table 6, all investigated compounds satisfy both the Born and dynamical stability criteria, thereby confirming their reliability under the studied conditions.

The formulations associated with the calculations of bulk modulus (B), shear modulus (G), Young's modulus (E), anisotropy (A), Poisson's ratio (v), Pugh's ratio (B/G), plasticity measurement (B/C_{44}), and Kleinman parameter (ς) were computed using the following expressions, respectively,[76–80]

$$B = \frac{1}{3}(C_{11} + 2C_{12}) \quad (7)$$

$$G = \frac{G_V + G_R}{2} \quad (8)$$

$$G_V = \frac{C_{11} - C_{12} + C_{44}}{5} \quad (9)$$

$$G_R = \frac{5C_{44}(C_{11} - C_{12})}{4C_{44} + 3(C_{11} - C_{12})} \quad (10)$$

Table 5 Pressure-dependent mechanical stability conditions for A_3CrO_4 (A = Mg, Ca, Sr)

Compounds	Pressure P (GPa)	Born stability at P = 0 (GPa)			Dynamical stability			Stability
		C_{11}	C_{44}	$C_{11} + 2C_{12}$	$C'_{11} - C'_{12}$	$C'_{11} + 2C'_{11}$	C'_{44}	Stable
Mg_3CrO_4	0	239.07	110.75	447.29	134.96	447.29	110.75	Stable
	20	343.78	114.08	492.88	249.68	492.88	94.08	Stable
	30	478.14	117.29	680.70	245.58	680.70	87.29	Stable
Ca_3CrO_4	0	214.37	74.05	339.65	151.73	339.65	74.05	Stable
	20	391.87	72.90	581.09	183.66	581.09	52.90	Stable
	30	466.44	74.19	657.38	245.97	657.38	44.19	Stable
Sr_3CrO_4	0	177.63	53.55	273.53	129.68	273.53	53.55	Stable
	20	362.99	48.90	529.83	176.15	529.83	28.90	Stable
	30	444.05	42.07	638.57	219.53	638.57	12.07	Stable

Table 6 The calculated elastic constants C_{ij} (GPa), bulk modulus B (GPa), shear modulus G (GPa), Young's modulus Y (GPa), Pugh's ratio G/B, and Poisson's ratio (ν) of the A_3CrO_4 compounds (A = Mg, Ca, Sr) under hydrostatic pressures of 0–30 GPa

	Mg_3CrO_4			Ca_3CrO_4			Sr_3CrO_4		
	0 GPa	20 GPa	30 GPa	0 GPa	20 GPa	30 GPa	0 GPa	20 GPa	30 GPa
Elastic constants C_{11} (GPa)	239.07	343.78	478.14	214.37	391.87	466.44	177.63	362.99	444.05
C_{12} (GPa)	104.11	74.55	101.28	62.64	94.61	95.47	47.95	83.42	97.26
C_{44} (GPa)	110.75	114.08	117.29	74.05	72.90	74.19	53.55	48.90	42.07
Bulk modulus B (GPa)	149.09	164.29	226.9	113.21	193.69	219.12	71.17	176.61	212.85
Poisson ratio ν	0.24	0.20	0.24	0.22	0.284	0.288	0.23	0.31	0.37
Shear modulus G (GPa)	90.79	121.89	141.94	74.77	97.37	108.16	45.07	75.67	77.47
Young modulus Y (GPa)	226.41	293.17	352.36	183.84	250.20	278.64	111.65	198.64	207.28
Anisotropy factor A	0.30	0.84	0.62	0.97	0.49	0.39	1.53	0.34	0.24
Pugh ratio B/G	1.64	1.34	1.59	1.51	1.98	2.02	1.57	2.33	2.74
Kleinman parameter	0.56	0.36	0.36	0.44	0.39	0.35	0.54	0.38	0.37
Nature	Brittle	Brittle	Brittle	Brittle	Ductile	Ductile	Brittle	Ductile	Ductile
Other calculation[46]	Mg_3FeO_4			Ca_3FeO_4			Sr_3FeO_4		
C_{11}	254.61			244.81			181.69		
C_{12}	102.51			57.60			51.81		
C_{44}	117.35			101.21			88.62		
Bulk modulus B (GPa)	153.21			120.01			95.10		
Poisson ratio ν	0.23			0.17			0.17		
Shear modulus G (GPa)	98.62			98.09			78.24		
Anisotropy factor A	1.54			1.08			1.36		
Pugh ratio B/G	1.53			1.22			1.21		
Kleinman parameter	0.54			0.38			0.43		
Nature	Brittle			Brittle			Brittle		

$$E = \frac{9BG}{(3B+G)} \tag{11}$$

$$A = \frac{2C_{44}}{C_{11}-C_{12}} \tag{12}$$

$$\nu = \frac{(3B-2G)}{2(3B+G)} \tag{13}$$

$$\zeta = \frac{C_{11}+8C_{12}}{7C_{11}+2C_{12}} \tag{14}$$

The elastic constants C_{11}, C_{12} and C_{44} provide fundamental insights into a material's response to external stress. For all three investigating compounds C_{11} significantly increases with pressure, as shown in Fig. 7(a), indicating enhanced resistance to uniaxial compression. This trend is typical for solids under pressure, as interatomic distances decrease, leading to stronger bonds and a stiffer lattice.[81] The increase in C_{12} and C_{44} also suggests increased resistance to shear deformation and improved shear stiffness under compression. The positive values of elastic constants across all the pressures satisfied the Born stability criteria of these cubic structures under the investigated conditions.

The bulk modulus representing resistance to volume change, consistently increases with pressure for all the compounds shown in Fig. 7(c). This indicates that all three compounds become significantly stiffer and less compressible under elevated pressure. The Young's modulus which measures stiffness also increases with pressure, reinforcing the observation of enhanced mechanical rigidity. Among the investigated compounds the Mg_3CrO_4 compounds are dominant throughout the pressure range shown in Fig. 7(b). These findings suggest that these chromates could potentially maintain their structural integrity in high-pressure environments making them candidates for applications requiring mechanically robust materials.[60]

Poisson's ratio, an elastic constant that describes how a material deforms sideways in response to longitudinal force, is also known as the transverse deformation coefficient. Poisson's ratio is a characteristic with a minimum value of approximately 0.26[82] in most metals. A Poisson's ratio greater than 0.25 suggests predominantly ionic bonding in the compound, whereas a value below 0.25 indicates predominantly covalent bonding.[83] The Poisson's ratio values indicate that Mg_3CrO_4 ($\nu < 0.25$) exhibits predominantly covalent bonding, whereas Ca_3CrO_4 and Sr_3CrO_4 ($\nu > 0.25$ at higher pressures) show a transition toward ionic bonding characteristics, consistent with their enhanced ductility under compression. For Mg_3CrO_4, Poisson's ratio fluctuates between 0.20 and 0.24 suggesting it remains relatively brittle. Ca_3CrO_4 shows an increase from 0.22 to 0.288 indicating a potential shift towards more ductile behavior at higher pressures. Notably, the Sr_3CrO_4 compound significantly increases from 0.23 at 0 GPa to 0.37 at 30 GPa pointing towards enhanced ductility under compression, as shown in Fig. 7(d). Ductile materials have potential applications in flexible electronics as well as photovoltaic cells, as the ability to sustain mechanical deformation without fracturing is needed.[84] This increasing ductility with pressure is a desirable characteristic for materials used in extreme conditions where resistance to fracture is critical.[60] Recent studies confirm that in perovskite oxides, applied pressure can induce a shift from covalent to ionic bonding, which enhances ductility and mechanical resilience critical for applications such as solid oxide fuel cells, thermoelectric, and spintronics.[85,86]

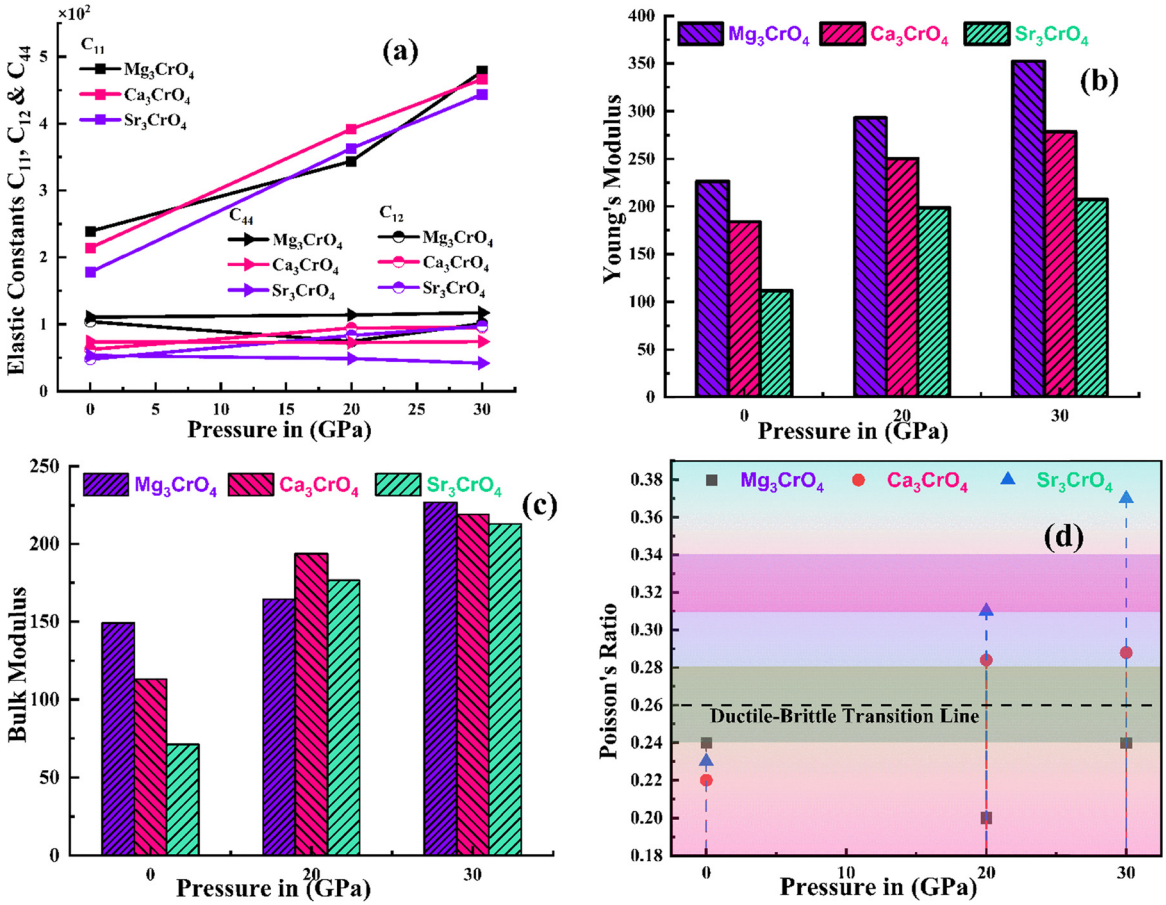

Fig. 7 (a–d) Variations in the elastic constants C_{ij}, Young's modulus, Bulk modulus and Poisson's ratio of the A_3CrO_4 compounds (A = Mg, Ca, Sr) under hydrostatic pressures of 0–30 GPa.

Agouri *et al.*[87] demonstrated through first-principles calculations on $PbXO_3$ (X = Ge, Si) perovskites that applied pressure induces a progressive shift from covalent to ionic bonding, thereby enhancing ductility and mechanical stability for energy applications. Similarly, Rahman *et al.*[88] reported pressure-induced transitions in Ba_3SbI_3 perovskites, where bonding changes under compression were directly linked to improved ductility and optoelectronic performance.

The bulk to shear modulus ratio (B/G) is another important indicator of ductility. A B/G ratio greater than 1.75 often correlates with ductile behavior while values less than 1.75 suggest brittleness. Both Mg_3CrO_4 compounds generally maintain B/G ratios below or around 1.75 indicating brittle behavior. In contrast, the B/G ratio of Ca_3CrO_4 and Sr_3CrO_4 compounds transit from brittle characteristics at 0 GPa and from 20 GPa to 30 GPa further supporting its transition to a ductile state under high pressure.

The Kleinman parameter is crucial for understanding the nature of interatomic forces with a material, particularly distinguishing between bond-stretching and bond bending contributions to the elastic response. A Kleinman parameter closer to 0 indicates that bond-bending forces are more significant, while a value closer to 1 suggests a predominance of bond-stretching forces. The calculated Kleinman parameters for Mg_3CrO_4, Ca_3CrO_4, and Sr_3CrO_4 reveal a consistent decrease with increasing hydrostatic pressure (0–30 GPa). At ambient conditions, values around 0.44–0.56 indicate a balanced contribution of bond stretching and bond bending to the elastic response. However, under compression, the parameters drop toward 0.35–0.37, signifying that bond bending becomes increasingly dominant suggesting a significant shift in the materials elastic behaviour: bond bending becomes increasingly dominant over bond stretching under compression.[89] This trend aligns with literature reports on perovskite oxides and halide crystals, where pressure enhances orbital overlap and shortens bond lengths, thereby favoring angular distortions over bond elongation. The persistence of stable Kleinman parameters across all pressures confirms the dynamical stability of these chromates, while the shift toward bond bending suggests enhanced mechanical flexibility. Such behavior is particularly relevant for piezoelectric and optoelectronic applications, where internal atomic displacements strongly influence polarization, optical absorption, and carrier transport.

2.5 Thermal properties and sound velocities

Thermodynamic stability is a fundamental requirement for materials intended for high-temperature applications, necessitating a comprehensive evaluation of their thermal behavior. Thermodynamics governs the principles of energy exchange

and heat flow within physical systems, and parameters such as Debye temperature (θ_D) and acoustic wave velocities serve as critical indicators of thermo-physical performance. Key properties including θ_D melting temperature (T_m) can be derived from longitudinal (V_l), transverse (V_t), and average sound velocities (v_m), in conjunction with material density (ρ), as detailed in Table 7. These sound velocities were calculated using established theoretical relationships and are presented in Table 7 and illustrated in Fig. 8.

$$V_m = \left[\left(\frac{1}{3}\right)\left(\frac{2}{V_t^3}+\frac{1}{V_l}\right)\right]^{-\frac{1}{3}} \quad (15)$$

$$V_t = \left(\frac{G}{\rho}\right)^{\frac{1}{2}} \quad (16)$$

$$V_l = \left(\frac{B}{\rho}+\frac{4G}{3\rho}\right) \quad (17)$$

The average sound velocity is directly related to the stiffness of the materials and speed at which phonons propagate through the lattice. From Table 7 and Fig. 8(d) the average sound velocity of Mg_3CrO_4 and Ca_3CrO_4 consistently increases with pressure. This trend indicates a stiffening of the crystal lattice and stronger interatomic bonds under compression which is consistent with the general increase in elastic moduli observed in such materials under pressure. Higher sound velocities typically correlate with higher Debye temperature and melting temperatures, suggesting improved thermal stability and mechanical integrity at elevated pressures. In contrast Sr_3CrO_4 exhibits a more complex behavior where the average sound velocity increases from 3721.06 at 0 GPa to 3898.81 at 20 GPa but then slightly decrease to 3765.56 at 30 GPa. This anomaly might be indicative of a pressure induced change in its electronic and magnetic configurations potentially related to the magnetic reversal observed in previously analyses for Sr_3CrO_4 under higher pressures.

The Debye temperature (θ_D) is a key parameter relating to the maximum vibration frequency of atoms in a crystal lattice, and is directly linked to material stiffness and thermal conductivity. Although not directly measurable, θ_D can be reliably estimated from elastic modulus data using the following expressions,[90]

$$\Theta_D = \frac{h}{K_B}\left[\frac{3n}{4\pi}\left(\frac{N_A\rho}{M}\right)\right]^{\frac{1}{3}} V_m \quad (18)$$

As presented in Table 7 and Fig. 8(a), the Debye temperature generally increases with pressure indicating a stiffening of the lattice and potentially improved thermal stability. J. Zhang *et al.*[91] and L. Zhang *et al.*[92] reported that the Debye temperature increases with applied pressure, thereby confirming the suitability of these compounds for high-temperature applications. The results in Table 7 clearly demonstrate that the Debye temperature (θ_D) of A_3CrO_4 compounds increases with applied pressure, consistent with previous reports. For Mg_3CrO_4, θ_D rises from 731.37 K at 0 GPa to 890.97 K at 30 GPa, representing a substantial increase of 159.6 K. Similarly, Ca_3CrO_4 shows an increase from 621.89 K to 717.48 K, while Sr_3CrO_4 increases from 445.70 K to 480.74 K over the same pressure range. This systematic enhancement of θ_D under compression indicates stronger interatomic bonding and greater lattice rigidity, confirming the suitability of these compounds for high-temperature applications, in agreement with previous results. At 30 GPa, Sr_3CrO_4 exhibits a reduction in Debye temperature, unlike Mg_3CrO_4 and Ca_3CrO_4. While Mounaim Bencheikh *et al.*[93] attributed decreases in θ_D at constant pressure to thermal expansion and lattice softening, this mechanism is unlikely under compression where volume expansion is suppressed. The more probable origin is a pressure-induced change in the magnetic state of Sr_3CrO_4 which modifies vibrational modes and reduces θ_D highlighting the role of magneto-elastic coupling in its lattice dynamics. Among them the Mg-based compounds exhibit the highest Debye temperatures among the materials studied, indicating stronger interatomic bonding and superior phonon-mediated thermal conductivity.[93]

The melting temperature plays a critical role in determining the thermal stability, performance, and applicability of materials across various scientific and industrial domains, including alloy design, nanoparticle stability, and high-temperature technologies.[94] The melting temperature (T_m) is calculated using the following relationship.[95]

$$T_m = 553 + 5.91C_{11} \quad (19)$$

As illustrated in Table 7 and Fig. 8(c), the melting temperature T_m is consistently predicted to increase significantly with pressure for all chromates. The calculated melting temperatures (T_m) of A_3CrO_4 compounds show a clear increasing trend with pressure, reflecting enhanced lattice stability under compression. For Mg_3CrO_4, T_m rises from 1965.90 K at 0 GPa to 3378.80 K at 30 GPa. Ca_3CrO_4 exhibits a similar increase, from

Table 7 GGA calculations of the Debye temperature (θ_D, K), average sound velocity (v_m, m s^{-1}), Debye frequency (ω_D, THz), melting temperature (T_m, K), and Gruneisen parameter (γ) of A_3CrO_4 compounds (A = Mg, Ca, Sr) under hydrostatic pressures of 0–30 GPa

	Mg_3CrO_4			Ca_3CrO_4			Sr_3CrO_4		
	0 GPa	20 GPa	30 GPa	0 GPa	20 GPa	30 GPa	0 GPa	20 GPa	30 GPa
Debye temperature θ_D	731.37	831.93	890.97	621.89	691.73	717.48	445.70	489.67	480.74
Average sound velocity	5252.09	5766.36	6085.84	4875.50	5204.24	5314.84	3721.06	3898.81	3765.56
Debye frequency ω_D	15.2	17.3	18.6	12.96	14.42	14.95	9.28	10.19	10.02
Melting temperature T_m	1965.90	2584.73	3378.80	1819.92	2868.95	3309.66	1248.19	2698.27	3177.33
Gruneisen parameter	1.066	1.003	1.058	1.041	1.23	1.28	1.05	1.16	1.20

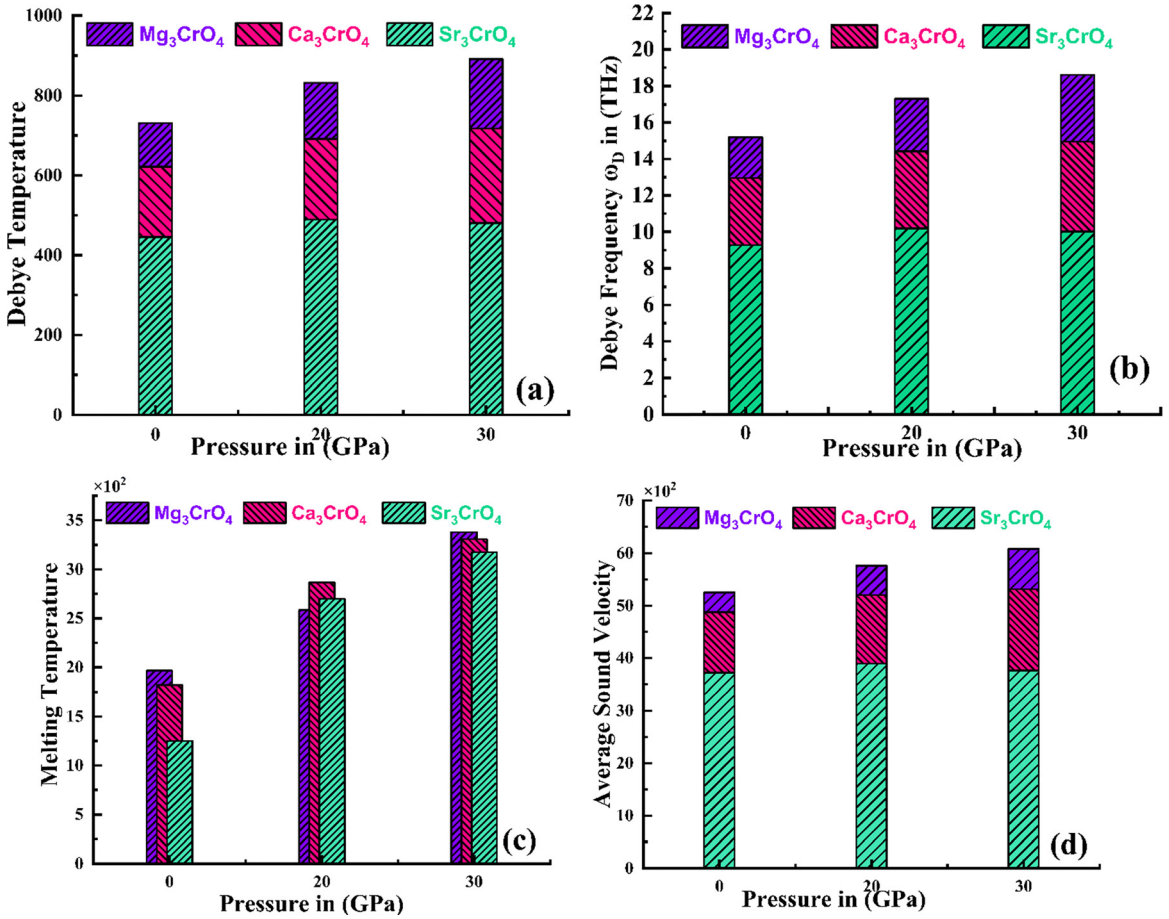

Fig. 8 (a–d) Variations in Debye temperature, average sound velocity, Debye frequency, and melting temperature of A_3CrO_4 compounds (A = Mg, Ca, Sr) under hydrostatic pressures of 0–30 GPa.

1819.92 K to 3309.66 K, while Sr_3CrO_4 shows the most pronounced change, from 1248.19 K to 3177.33 K over the same pressure range. These results indicate that hydrostatic compression significantly strengthens interatomic bonding, thereby elevating the melting point.[96] The systematic increase in T_m confirms the suitability of these compounds for high-temperature applications, consistent with literature reports that pressure enhances thermal stability in oxide materials.[97] This strong correlation between pressure and melting temperature suggests that these materials can withstand much higher temperatures at elevated pressures which is a critical consideration for high temperature and high-pressure applications. Such high melting points are characteristic of robust ceramic materials.[60]

The Debye frequency (ω_D) is a measure of the maximum vibrational frequency of atoms in a crystal lattice serving as a fundamental parameter in solid-state physics for understanding thermal properties. The Debye frequency for a given solid is calculated using the following expression.[94]

$$\omega_D = K_B.\frac{\theta_D}{h} \quad (20)$$

From Table 7 and Fig. 8(b), the Debye frequency of Mg_3CrO_4 increases from 15.2 THz at 0 GPa to 18.6 THz at 30 GPa. Similarly, the Debye frequency of Ca_3CrO_4 also shows an increase from 12.96 THz to 14.95 THs. This increase signifies an enhanced stiffness of the phonon nodes under pressure implying a stronger lattice that can sustain higher frequency vibrations. Fr Sr_3CrO_4 the Debye frequency increases from 9.28 THz at 0 GPa to 10.19 THz at 20 GPa but then slightly decrease to 10.02 THz at 30 GPa, mirroring the trend observed in its average sound velocity. This behavior reinforces the hypothesis of pressure induced events affecting the lattice dynamics of Sr_3CrO_4.[98] Materials with higher Debye frequencies are generally expected to have higher thermal conductivities and specific heats making these chromates potentially suitable for applications requiring efficient heat dissipation of thermal insulation under specific conditions.

Table 7 also reports the Gruneisen parameter (γ), which quantifies the anharmonicity of the lattice vibrations and the relationship between thermal expansion and changes in vibrational frequencies with volume. It is a parameter for understanding a materials thermal expansion coefficient and its response to temperature changes under pressure. This parameter is derived from Poisson's ratio using the following relationship.[99]

$$\gamma = \frac{3(1+v)}{2(2-3v)} \quad (21)$$

The calculated values for investigated compounds under pressure remain close to unity, indicating moderate anharmonicity. A positive Gruneisen parameter implies that phonon frequencies increase upon compression, which is typical for most solids. The variations in this parameter provide insights into how each material's thermal properties will respond to external pressure, influencing applications where thermal stability and dimensional changes are critical. The observed increase in γ with pressure for Ca_3CrO_4 and Sr_3CrO_4 is consistent with literature reports by Mounaim Bencheikh *et al.*[93] showing that compression amplifies anharmonic lattice responses by modifying phonon frequencies. In contrast, Mg_3CrO_4 shows only weak variation, suggesting greater anharmonic stability under hydrostatic compression. Overall, the results confirm that pressure enhances anharmonic effects in A_3CrO_4 compounds, while the magnitude of γ remains within the range typical for stable oxide materials. For instance, materials with low Gruneisen parameters tend to have low thermal expansion coefficients, desirable for precision components operating over wide temperature ranges.[100]

The observed pressure induced magnetic transition in our investigated compounds in the magnetic data discussed previously alongside the elastic property changes further emphasizes the intricate interplay between structural, electronic, elastic, thermodynamics and magnetic degrees of freedom in these materials.

In conclusion, the variations in average sound velocity, Debye frequency, and Gruneisen parameter with pressure provide a comprehensive picture of the lattice dynamics and thermal behavior of Mg_3CrO_4, Ca_3CrO_4 and Sr_3CrO_4. The consistent stiffening and enhanced thermal stability observed in Mg_3CrO_4 and Ca_3CrO_4 make them promising for high-pressure and high-temperature applications. The anomalous behavior of Sr_3CrO_4, particularly the decrease in sound velocity and Debye frequency at higher pressures, suggests a pressure-induced phenomenon that requires further investigation, potentially leading to new applications in pressure-tunable functional materials. These findings contribute to the broader understanding of complex oxides and their potential in advancing materials science and engineering.

3. Conclusion

This study delivers a comprehensive DFT-based exploration of A_3CrO_4 (A = Mg, Ca, Sr) chromates under hydrostatic pressures up to 30 GPa, employing GGA-PBE, GGA-PBEsol, and GGA+U functionals to capture their structural, electronic, magnetic, elastic, and thermal responses. Mg_3CrO_4 and Ca_3CrO_4 consistently retain ferromagnetic half-metallicity, exhibit lattice stiffening, rising Debye temperatures and frequencies, and increasing melting points, confirming their robustness for high-temperature and high-pressure applications. Sr_3CrO_4, in contrast, shows anomalous pressure-dependent behavior, including magnetic moment reversal and reductions in sound velocity and Debye frequency at higher pressures, pointing to a unique pressure-induced phase transition. Elastic constant analysis verifies dynamic stability across all compounds, with ductility transitions observed in Ca_3CrO_4 and Sr_3CrO_4 under compression. Electronic structure calculations further reveal persistent half-metallicity across all compounds, with spin-down channels maintaining wide band gaps and spin-up channels displaying metallic behavior. The inclusion of Hubbard corrections (GGA+U) strengthens the reliability of these electronic predictions, confirming the robustness of the band structure and magnetic ordering. Collectively, these results establish Mg_3CrO_4 and Ca_3CrO_4 as promising candidates for spin-injection layers and ceramic applications, while Sr_3CrO_4 emerges as a potential pressure-tunable functional material. Overall, the findings advance the understanding of complex oxides and highlight their potential in next-generation spintronic and high-performance technologies.

Conflicts of interest

There are no conflicts to declare.

Data availability

The data supporting the findings of this study, including structural parameters, magnetic moments, elastic, and electronic band structures of A_3CrO_4 (A = Mg, Ca, Sr) alkali–metal oxides are available from the corresponding author upon reasonable request. No restrictions apply to data sharing.

References

1 J. T. Gish, D. Lebedev, T. W. Song, V. K. Sangwan and M. C. Hersam, van der Waals opto-spintronics, *Nat. Electron.*, 2024, **7**, 336–347.
2 Y. Niu, Y. Wang, L. Wang, Y. Sun and P. Wang, Unveiling the spin polarization mechanism in half-metallic CrO2 regulated by crystal plane orientation, *New J. Chem.*, 2025, **49**, 17802–17807.
3 J. F. Sierra, J. Fabian, R. K. Kawakami, S. Roche and S. O. Valenzuela, van der Waals heterostructures for spintronics and opto-spintronics, *Nat. Nanotechnol.*, 2021, **16**, 856–868.
4 V. Chaudhary, *et al.*, Spin and current transport in the robust half-metallic magnet c-CoFeGe, *J. Phys.: Condens. Matter*, 2023, **35**, 285502.
5 K. Peng, *et al.*, A DFT study on half-metallicity of Ruddlesden–Popper layered perovskite $Bi_8Ba_4Mn_8O_{28}$, *Phys. B*, 2024, **674**, 415587.
6 I. C. Oguz, F. Jaouen and T. Mineva, Exploring Spin Distribution and Electronic Properties in FeN4-Graphene Catalysts with Edge Terminations, *Molecules*, 2024, **29**(2), 479.
7 X. P. Wei, Z. Y. Mei and X. Tao, Surface effects for half-metallic Heusler alloy CrYCoAl, *Phys. B*, 2024, **683**, 415925.
8 Y. Zou, *et al.*, First-Principles Study on Mechanical, Electronic, and Magnetic Properties of Room Temperature

Ferromagnetic Half-Metal MnNCl Monolayer, *Nanomaterials*, 2023, **13**(11), 1712.

9 X. Hu, Half-metallic antiferromagnet as a prospective material for spintronics, *Adv. Mater.*, 2012, **24**, 294–298.

10 P. Mavropoulos, M. Ležaić and S. Blügel, Half-metallic ferromagnets for magnetic tunnel junctions by ab initio calculations, *Phys. Rev. B: Condens. Matter Mater. Phys.*, 2005, **72**, 174428.

11 M. Shaughnessy, R. Snow, L. Damewood and C. Y. Fong, Memory and Spin Injection Devices Involving Half Metals, *J. Nanomater.*, 2011, 140805.

12 S. M. Yakout, Spintronics: Future Technology for New Data Storage and Communication Devices, *J. Supercond. Novel Magn.*, 2020, **33**, 2557–2580.

13 S. S. P. Parkin, *et al.*, Exchange-biased magnetic tunnel junctions and application to nonvolatile magnetic random access memory (invited), *J. Appl. Phys.*, 1999, **85**, 5828–5833.

14 R. A. De Groot, F. M. Mueller, P. G. V. Engen and K. H. J. Buschow, New Class of Materials: Half-Metallic Ferromagnets, *Phys. Rev. Lett.*, 1983, **50**, 2024.

15 A. Fakhim Lamrani, *et al.*, Half metallic antiferromagnetic behavior in doped TiO2 rutile with double impurities (Os, Mo) from ab initio calculations, *Thin Solid Films*, 2014, **570**, 45–48.

16 J. A. G. Cerón, D. A. L. Téllez and J. Roa-Rojas, Weak Ferromagnetism in the $FeCr_2O_4$ Semiconductor Spinel with Half-Metallic Feature in the Ground State, *J. Electron. Mater.*, 2021, **51**, 822–830.

17 L. Feng, F. Wang, J. Li and S. J. Wang, A First-Principles Study of Half-Metallic Full-Heusler Compound Ti_2CoSi, *Appl. Mech. Mater.*, 2013, **320**, 394–398.

18 W. T. Chen, *et al.*, A half-metallic A- and B-site-ordered quadruple perovskite oxide $CaCu_3Fe_2Re_2O_{12}$ with large magnetization and a high transition temperature, *Nat. Commun.*, 2014, **5**, 1–7.

19 K. Yi, Q. Tang, Z. Wu, J. Gu and X. Zhu, Structural, magnetic, and electrical transport properties of half-metallic double perovskite La_2CrNiO_6 oxides, *J. Alloys Compd.*, 2023, **933**, 167742.

20 S. A. Dar, V. Srivastava and U. K. Sakalle, Structural, elastic, mechanical, electronic, magnetic, thermoelectric and thermodynamic investigation of half metallic double perovskite oxide Sr_2MnTaO_6, *J. Magn. Magn. Mater.*, 2019, **484**, 298–306.

21 A. Kumar, M. Kumar and R. P. Singh, Magnetic, optoelectronic, and thermodynamic properties of half-metallic double perovskite oxide, Ba_2YbTaO_6: a density functional theory study, *J. Mater. Sci.: Mater. Electron.*, 2021, **32**, 12951–12965.

22 Y. Chen, *et al.*, Density Functional Theory Study of Nonvolatile Electrical Control of Half-Metallicity in Multiferroic $RuCl_2/Al_2S_3$ Heterostructures: Implications for Spin Memory Devices, *ACS Appl. Nano Mater.*, 2024, **7**, 4302–4312.

23 C. Jin, *et al.*, Ferroelectric modulated giant valley polarization and half metallicity in 2D $RuBrF/Sc_2CO_2$ multiferroic heterostructure for non-volatile memory applications, *J. Appl. Phys.*, 2025, **138**, 064504.

24 U. Hameed, *et al.*, First-principles calculations to investigate magnetic, electronic, and thermoelectric response of europium-based half metallic ternary Zintl compounds $EuMg_2X_2$ (X = Sb and Bi), *J. Phys. Chem. Solids*, 2025, **199**, 112519.

25 Z. Zada, *et al.*, Structure stability, half metallic ferromagnetism, magneto-electronic and thermoelectric properties of new zintl XCr_2Bi_2 (X = Ca, Sr) compounds for spintronic and renewable energy applications, *Phys. B*, 2021, **607**, 412866.

26 B. Balke, *et al.*, Doped semiconductors as half-metallic materials: Experiments and first-principles calculations of Co $Ti_{1-x}M_xSb$ (M = Sc, V, Cr, Mn, Fe), *Phys. Rev. B: Condens. Matter Mater. Phys.*, 2008, **77**, 045209.

27 S. Seong, *et al.*, Experimental evidence for mixed-valent Cr ions in half-metallic CrO2: Temperature-dependent XMCD study, *J. Magn. Magn. Mater.*, 2018, **452**, 447–450.

28 S. Barouni, *et al.*, First-principles prediction of half metallic-ferromagnetism in $La_{0.25}Sr_{0.75}Sn_{0.4}In_{0.25}Ru_{0.35}O_3$ and enhanced experimental electrical and magnetic behaviours, *Phys. Chem. Chem. Phys.*, 2024, **26**, 18102–18112.

29 R. A. Parray and K. Ravichandran, Experimental studies of Cr_2NiAl half-metallic inverse Heusler compound for spintronic applications, *J. Mater. Sci.: Mater. Electron.*, 2023, **34**, 1–10.

30 O. Ramdane, M. Labidi, S. Labidi and R. Masrour, A comparative study on the structural, electronic, and magnetic properties of the cubic Sr-based perovskite $SrXO_3$ (X = Mn, Sn, Cr): DFT calculation, *J. Korean Ceram. Soc.*, 2024, **61**, 993–1005.

31 M. Jamil, *et al.*, A DFT theoretical prediction of new half-metallic ferromagnetism, mechanical stability, optoelectronic and thermoelectric properties of ZnCrO3 perovskites for spintronic applications, *Solid State Commun.*, 2024, **394**, 115702.

32 N. Erum, *et al.*, First-principles studies on physical properties for new half-metallic perovskites AFeO3 (A = Ca, Sr, Ba): Spintronics and energy harvesting applications, *Int. J. Quantum Chem.*, 2024, **124**, e27363.

33 K. Prateek, *et al.*, Magnetotransport properties of CrO2 nanowires fabricated by selective area growth, *J. Phys. Chem. Solids*, 2023, **178**, 111350.

34 A. E. Aly and D. P. Rai, A DFT Study of Electronic and Magnetic Properties of Cr 2 O 3 using Spin-Polarized Approach, *Int. J. Comput. Phys. Ser.*, 2018, **11**, 91–96.

35 B. H. Rimmler, B. Pal and S. S. P. Parkin, Non-collinear antiferromagnetic spintronics, *Nat. Rev. Mater*, 2025, **10**, 109–127.

36 M. E. A. Monir, *et al.*, Structural, elastic, electronic, magnetic and thermal properties of X_3FeO_4 (X = mg, ca and Sr) materials, *Sci. Rep.*, 2025, **15**, 2957.

37 J. P. Perdew and A. Zunger, Self-interaction correction to density-functional approximations for many-electron systems, *Phys. Rev. B: Condens. Matter Mater. Phys.*, 1981, **23**, 5048.

38 D. M. Ceperley and B. J. Alder, Ground State of the Electron Gas by a Stochastic Method, *Phys. Rev. Lett.*, 1980, **45**, 566.
39 M. D. Segall, *et al.*, First-principles simulation: ideas, illustrations and the CASTEPcode, *J. Phys.: Condens. Matter*, 2002, **14**, 2717.
40 B. G. Pfrommer, M. Côté, S. G. Louie and M. L. Cohen, Relaxation of Crystals with the Quasi-Newton Method, *J. Comput. Phys.*, 1997, **131**, 233–240.
41 B. Banik, M. Shamima Khanom, M. R. Hossain and F. Ahmed, Computational evaluation of pressure effects on cubic ferromagnetic perovskites ACrBr3 (A = K, Rb, Cs, Fr): materials engineering perspectives for spintronics and optoelectronics via DFT, *Mater. Adv.*, 2026, **7**, 4307–4328.
42 M. C. Payne, M. P. Teter, D. C. Allan, T. A. Arias and J. D. Joannopoulos, Iterative minimization techniques for ab initio total-energy calculations: molecular dynamics and conjugate gradients, *Rev. Mod. Phys.*, 1992, **64**, 1045.
43 S. Vensky, *et al.*, The real structure of Na_3BiO_4 by electron microscopy, HR-XRD and PDF analysis, *Z. Kristallogr.*, 2005, **220**, 231–244.
44 M. E. A. Boulekbache, *et al.*, Structural, magnetic, electronic, and thermodynamic properties of Ba_2ScMO_6 (M = Ru, Os) double perovskites, *J. Mater. Sci.*, 2026, 1–14, DOI: 10.1007/S10853-026-12725-9.
45 S. Belhachi, *et al.*, DFT Analysis of Ba 2 NbRhO 6: A Promising Double Perovskite for Sustainable Energy Applications, *J. Inorg. Organomet. Polym. Mater.*, 2025, **35**, 978–993.
46 M. E. A. Monir, *et al.*, Structural, elastic, electronic, magnetic and thermal properties of X_3FeO_4 (X = mg, ca and Sr) materials, *Sci. Rep.*, 2025, **15**, 2957.
47 M. Y. Sofi, M. S. Khan and M. A. Khan, *Mater. Adv.*, 2024, 4913–4931, DOI: 10.1039/d3ma01160g.
48 S. Nazir, *et al.*, Investigation of Opto-Electronic and Thermoelectric Characteristics of Halide Perovskite CdLiCl3 for Energy Conversion Applications at Different Pressure, *J. Inorg. Organomet. Polym. Mater.*, 2024, **35**, 493–502.
49 S. Ahmad Khandy and D. C. Gupta, DFT analogue of prospecting the spin-polarised properties of layered perovskites Ba 2 ErNbO 6 and Ba 2 TmNbO 6 influenced by electronic structure, *Sci. Rep.*, 2022, **12**, 19690.
50 S. Gautam, S. Ghosh and D. C. Gupta, Understanding the computational insights of spin-polarised density functional theory into the newly half-metallic f electron-based actinide perovskites $SrMO_3$ (M = Pa, Np, Cm, Bk), *Sci. Rep.*, 2023, **13**, 16882.
51 F. Firdous, *et al.*, Half-metallicity, magnetic and optical attributes of mechanically stable half-Heusler VSnX (X = Pt, Pd) alloys for spintronics: a DFT study, *Eur. Phys. J. Plus*, 2023, **138**, 699.
52 M. Ahmad, *et al.*, Intrinsic Room-Temperature Ferromagnetism in New Halide Perovskite AgCrX3 (X: F, Cl, Br, I) Using Ab Initio and Monte Carlo Simulations, *ACS Omega*, 2024, **9**, 18148–18159.
53 R. Islam and J. P. Borah, Electronic structure and magnetic properties investigation of cubic Fe_3O_4, *Mater. Today Proc.*, 2022, **68**, 159–162.
54 J. Chang, *et al.*, On the electronic structure and magnetism of $CaCrO_3$: A hybrid-exchange density-functional-theory study, *Mater. Today Commun.*, 2021, **27**, 102179.
55 H. Ullah, *et al.*, Mechanical and magneto-electronic properties of europium lanthanide-based cubic perovskites EuYO3 (Y = Cr, Mn, Fe): An ab initio study, *J. Rare Earths*, 2024, **42**, 562–569.
56 O. Kabi, *et al.*, Ab Initio Investigation of the Structural, Elastic, Dynamic, Electronic, and Magnetic Properties of Cubic Perovskite $CeCrO_3$, *ACS Omega*, 2024, **9**, 11820–11828.
57 M. Agouri, *et al.*, First-principles calculations to investigate structural, electronic, elastic and thermodynamic properties of $PbXO_3$ (X = Ge, Si) perovskites under pressure effect for energy applications, *Chem. Pap.*, 2025, **80**, 1387–1398.
58 S. Nazir, A. A. Algethami and M. Musa Saad, Evolution of metallicity, enhancement of TC and magnetic anisotropy energy in Y_2NiIrO_6: Hydrostatic ([111]) strain influence, *J. Phys. Chem. Solids*, 2025, **197**, 112410.
59 J. Shi, G. W. Fernando, Y. Dang, S. L. Suib and M. Jain, Structural and electronic properties of rare-earth chromites: A computational and experimental study, *Phys. Rev. B*, 2022, **106**, 165117.
60 H. Ullah, *et al.*, Mechanical and magneto-electronic properties of europium lanthanide-based cubic perovskites EuYO3 (Y = Cr, Mn, Fe): An ab initio study, *J. Rare Earths*, 2024, **42**, 562–569.
61 Y. Bouldiab, *et al.*, Strong half-metallic ferromagnetism and thermoelectric response in new half-Heusler RbCrX (X = Sb, As) alloys: first-principles calculations, *Indian J. Phys.*, 2021, **96**, 2755–2778.
62 N. A. N. M. Nor, *et al.*, Influence of Hubbard U correction on the structural, electronic and optical properties of Kesterite Cu_2XSnS_4 (X= Zn, Fe), *Phys. B*, 2024, **673**, 415450.
63 G. Shen, *et al.*, The first principle research of CaO and MgO particulate heterogeneous nucleation in Mg alloys, *Appl. Surf. Sci.*, 2022, **593**, 153224.
64 O. Ramdane, M. Labidi, S. Labidi and R. Masrour, A comparative study on the structural, electronic, and magnetic properties of the cubic Sr-based perovskite SrXO3(X = Mn, Sn, Cr): DFT calculation, *J. Korean Ceram. Soc.*, 2024, **61**, 993–1005.
65 Y. El-harrar, *et al.*, Study of optoelectronics and magnetic properties of GdCrWO6 oxide by ab initio calculations, *Comput. Condens. Matter*, 2024, **38**, e00859.
66 S. Tiwari and A. Mishra, Effect of Ionic Radii Variation on the Structural, Electrical, Dielectric, and Magnetic Characteristics of Orthochromite RCrO3 (R = La, Y, Gd), *J. Supercond. Novel Magn.*, 2024, **37**, 623–637.
67 W. Su, *et al.*, Structure and magnetic properties of electrospun rare earth orthochromites nanofibers, *Solid State Sci.*, 2023, **145**, 107314.
68 M. Schecter, O. F. Syljuåsen and J. Paaske, Nematic Bond Theory of Heisenberg Helimagnets, *Phys. Rev. Lett.*, 2017, **119**, 157202.

69 L. Yang, *et al.*, Absence of spin transport in amorphous YIG evidenced by nonlocal spin transport experiments, *Phys. Rev. B*, 2021, **104**, 144415.
70 A. Jabar, S. Benyoussef and L. Bahmad, Study of Physical Characteristics of the New Half-Heusler Alloy BaHgSn by DFT Analysis, *arXiv*, 2024, preprint, arXiv:2403.08483, DOI: 10.48550/arXiv.2403.08483, https://arxiv.org/pdf/2403.08483.
71 R. A. De Groot, F. M. Mueller, P. G. V. Engen and K. H. J. Buschow, New Class of Materials: Half-Metallic Ferromagnets, *Phys. Rev. Lett.*, 1983, **50**, 2024.
72 R. K. Pingak, *et al.*, Structural, Electronic, Elastic, and Optical Properties of Cubic BaLiX 3 (X = F, Cl, Br, or I) Perovskites: An Ab-initio DFT Study, *Indones. J. Chem.*, 2023, **23**, 843–862.
73 Z. J. Wu, *et al.*, Crystal structures and elastic properties of superhard Ir N2 and Ir N3 from first principles, *Phys. Rev. B: Condens. Matter Mater. Phys.*, 2007, **76**, 054115.
74 S. Goumri-Said and M. B. Kanoun, Theoretical investigations of structural, elastic, electronic and thermal properties of Damiaoite PtIn2, *Comput. Mater. Sci.*, 2008, **43**, 243–250.
75 J. Gao, Q. J. Liu and B. Tang, Elastic stability criteria of seven crystal systems and their application under pressure: Taking carbon as an example, *J. Appl. Phys.*, 2023, **133**, 135901.
76 M. J. Mehl, Pressure dependence of the elastic moduli in aluminum-rich Al-Li compounds, *Phys. Rev. B: Condens. Matter Mater. Phys.*, 1993, **47**, 2493.
77 Z. Sun, S. Li, R. Ahuja and J. M. Schneider, Calculated elastic properties of M_2AlC (M = Ti, V, Cr, Nb and Ta), *Solid State Commun.*, 2004, **129**, 589–592.
78 C. Jasiukiewicz and V. Karpus, Debye temperature of cubic crystals, *Solid State Commun.*, 2003, **128**, 167–169.
79 P. Wachter, M. Filzmoser and J. Rebizant, Electronic and elastic properties of the light actinide tellurides, *Phys. B*, 2001, **293**, 199–223.
80 M. J. Mehl, J. E. Osburn, D. A. Papaconstantopoulos and B. M. Klein, Structural properties of ordered high-melting-temperature intermetallic alloys from first-principles total-energy calculations, *Phys. Rev. B: Condens. Matter Mater. Phys.*, 1990, **41**, 10311.
81 G. Shen, *et al.*, The first principle research of CaO and MgO particulate heterogeneous nucleation in Mg alloys, *Appl. Surf. Sci.*, 2022, **593**, 153224.
82 M. A. Ali, *et al.*, Modeling of structural, elastic, mechanical, acoustical, electronic and thermodynamic properties of XPdF3 (X = Rb, Tl) perovskites through density functional theory, *Phys. Scr.*, 2020, **95**, 075705.
83 O. Kabi, *et al.*, Ab Initio Investigation of the Structural, Elastic, Dynamic, Electronic, and Magnetic Properties of Cubic Perovskite CeCrO3, *ACS Omega*, 2024, **9**, 11820–11828.
84 B. Banik, M. Shamima Khanom, M. R. Hossain and F. Ahmed, Computational evaluation of pressure effects on cubic ferromagnetic perovskites ACrBr 3 (A = K, Rb, Cs, Fr): materials engineering perspectives for spintronics and optoelectronics via DFT, *Mater. Adv.*, 2026, **52**, 115184.
85 X. Li, *et al.*, High pressure and Ti promote oxygen vacancies in perovskites for enhanced thermoelectric performance, *J. Alloys Compd.*, 2022, **922**, 166247.
86 K. Hilpert, *et al.*, Defect formation and mechanical stability of perovskites based on LaCrO3 for solid oxide fuel cells (SOFC), *J. Eur. Ceram. Soc.*, 2003, **23**, 3009–3020.
87 M. Agouri, *et al.*, First-principles calculations to investigate structural, electronic, elastic and thermodynamic properties of PbXO3 (X = Ge, Si) perovskites under pressure effect for energy applications, *Chem. Pap.*, 2025, **80**, 1387–1398.
88 M. F. Rahman, *et al.*, A novel investigation of pressure-induced semiconducting to metallic transition of lead free novel Ba 3 SbI 3 perovskite with exceptional optoelectronic properties, *RSC Adv.*, 2024, **14**, 11169–11184.
89 H. J. Alathlawi, *et al.*, Pressure-Induced Effects on BaPbO3: A Prospectively Valuable Material for Piezoelectric Applications via DFT, *Cryst. Res. Technol.*, 2024, **59**, 2300293.
90 O. L. Anderson, A simplified method for calculating the Debye temperature from elastic constants, *J. Phys. Chem. Solids*, 1963, **24**, 909–917.
91 J. Zhang, *et al.*, Electronic structure, mechanical, optical and thermodynamic properties of cubic perovskite InBeF3 with pressure effects: First-principles calculations, *Results Phys.*, 2023, **50**, 106590.
92 L. Zhang, *et al.*, Structural stability, mechanical, and thermodynamic properties under pressure of B2-type CuM (M = Be, Al, and Zn) alloys: a DFT investigation, *Phys. Scr.*, 2024, **99**, 065946.
93 M. Bencheikh and L. El Farh, First-principles study of the thermodynamic properties of the bulk cubic compound InTe at high temperature and pressure, *Next Mater.*, 2025, **9**, 101254.
94 M. Tarekuzzaman, *et al.*, DFT analysis of structural, electronic, optical, and thermodynamic properties of LiXI3 (where X = Ca, Sr, Ba) halide perovskites for optoelectronics, *Sci. Rep.*, 2025, **15**, 1–23.
95 M. E. Fine, L. D. Brown and H. L. Marcus, Elastic constants versus melting temperature in metals, *Scr. Metall.*, 1984, **18**, 951–956.
96 T. Özer and N. Arıkan, The Implications of Pressure on Mechanical and Thermodynamic Properties of Ni_2X (X = Sc, Ti, V)Al: DFT Calculation, *Russ. J. Phys. Chem. A*, 2024, **98**, 669–682.
97 S. A. Dar, V. Srivastava and U. K. Sakalle, Ab Initio High Pressure and Temperature Investigation on Cubic PbMoO3 Perovskite, *J. Electron. Mater.*, 2017, **46**, 6870–6877.
98 H. Jebari, *et al.*, First-principles calculations to investigate structural, electronic, optical, thermoelectric, magnetic, and magnetocaloric properties of the orthochromite EuCrO3, *Comput. Theor. Chem.*, 2023, **1220**, 113993.
99 D. R. Clarke, Materials selections guidelines for low thermal conductivity thermal barrier coatings, *Surf. Coat. Technol.*, 2003, **163–164**, 67–74.
100 S. Satapathy, M. Batouche, T. Seddik, M. M. Salah and K. K. Maurya, First Principle Study on Structural, Thermoelectric, and Magnetic Properties of Cubic CdCrO3 Perovskites: A Comprehensive Analysis, *Crystals*, 2023, **13**(8), 1185.